Laser-induced core-polarization effects in high-order harmonic generation from solids

Wanzhu He,[1] Ning Sun,[1] Xiaosong Zhu,[1,2,*] Liang Li,[1,†] Pengfei Lan,[1,2,‡] and Peixiang Lu[1,3,2]

[1]*Wuhan National Laboratory for Optoelectronics and School of Physics, Huazhong University of Science and Technology, Wuhan 430074, China*

[2]*Hubei Optical Fundamental Research Center, Wuhan 430074, China*

[3]*Hubei Key Laboratory of Optical Information and Pattern Recognition, Wuhan Institute of Technology, Wuhan 430205, China*

(Received 3 November 2023; revised 7 June 2024; accepted 15 July 2024; published 8 August 2024)

Under intense laser fields, atoms undergo core polarization, i.e., redistribution of the electron density around the nucleus. We systematically investigate the effect of core polarization on high-order harmonic generation (HHG) from solids using time-dependent density-functional theory in a laser-driven linear chain of atoms. It is shown that the presence of core polarization induces substantial variations in HHG compared with the results with a frozen core. Our study further provides insight into these phenomena by combining an approach that distinguishes the effects of core polarization from different shells and compares the contributions of inner and outer shells. Ultimately, we propose and demonstrate a two-color pump-probe scheme to effectively control the core-polarization effects, specifically by activating inner-shell electrons. This work highlights the significance of multielectron effects for solids and demonstrates the feasibility of manipulating the physical properties of materials through core polarization.

DOI: 10.1103/PhysRevA.110.023104

I. INTRODUCTION

High-order harmonic generation (HHG) is one of the nonlinear optical phenomena in intense laser-matter interactions [1,2]. The HHG in the gas phase laid the foundation for attosecond science [3,4]. Recently, the strong-field response in solids, in particular, HHG from solids, has captured considerable interest [5–9]. The HHG in solids not only presents a promising avenue for generating extreme ultraviolet radiation sources but also paves the way for groundbreaking advancements in the field of ultrafast optics [10–13]. Moreover, HHG serves as a powerful tool for elucidating the intrinsic electric structure of crystals and investigating the underlying dynamics of their internal electrons [14–21].

Currently, most studies of HHG from solids are rooted in the single-active-electron (SAE) approximation, which assumes that the active electron experiences a constant effective potential or moves within an energy band structure obtained in the absence of an external field. Correspondingly, the single-electron time-dependent Schrödinger equation (TDSE) and the semiconductor Bloch equations based on the SAE model are widely employed in contemporary works exploring the interaction between intense lasers and solid materials [14,22–28]. Based on the aforementioned models, many studies have explained various characteristics of HHG from solids, such as the multiplateau structure and cutoff dependence. In order to pursue going beyond the SAE models, first-principles numerical methods such as the time-dependent density-functional theory (TDDFT) and the time-dependent Hartree-Fock theory have also been utilized [29–34]. More recently, there has been related work on the semiconducting Bloch equations imposing a Hartree-Fock level of theory [35]. These methods take multielectron dynamics into account.

However, the multielectron effects, which have garnered significant attention in the study of atomic and molecular systems [36–46], still require further investigation in solids. Some studies found that the SAE approximation, utilized in many models, proves reasonable for bulk crystals or materials featuring model potentials [29,47]. Meanwhile, electron-electron interactions have been found to play a significant role in scenarios involving edges or defects breaking the translational symmetry [30,32,48–51]. These interactions often lead to suppression of the generated harmonics, a phenomenon explicable through the perspective of local-field effects in solid-state physics. Notably, Li *et al.* discovered core-polarization effects in HHG from MgO, without any limitations imposed by boundaries or symmetry breaking in their study [52]. This study was based on a four-step model for solid-state HHG, introducing scattering terms phenomenologically to simulate core-polarization effects. They focused on using a theoretical model to explain the experimental observations, i.e., anisotropic HHG structures in MgO, revealing the core polarization in the two-dimensional (2D) field.

In this study we adopt the definition from Ref. [52], where the atomic nucleus and all bound electrons were considered as a unified entity referred to as the core. When exposed to an intense laser, the electrons within the core exhibit a response by redistributing the charge density in the vicinity of the atom, known as core polarization. The core polarization consequently leads to changes in the effective potential, thereby influencing the dynamic behavior of the excited electrons

*Contact author: zhuxiaosong@hust.edu.cn
†Contact author: liangl@hust.edu.cn
‡Contact author: pengfeilan@hust.edu.cn

and ultimately regulating the radiation properties. The concept of core polarization mentioned in this work encompasses the effects arising from Coulomb interactions and exchange-correlation effects among bound electrons, which occur in a wide range of scenarios closely related to several types of multielectron phenomena mentioned earlier. However, systematic studies on this effect are relatively scarce in current research, indicating the need for further comprehensive investigations.

Our study proposes a subshell polarization approach to investigate the core-polarization effects. This approach allows us to focus separately on the effects caused by the polarization of a given shell. We demonstrate that core polarization induces a certain degree of harmonics suppression in a broad region across the first plateau. Additionally, core polarization causes a peak in a narrow spectral region in the HHG. The narrow region precisely corresponds to the energy gap between the highest valence band and the inner valence band. Combined with analyses including spatial-frequency analysis, time-frequency analysis, and channel analysis, we examine the characteristics and radiative properties of these two phenomena. Ultimately, based on the results of the subshell analyses, we propose a two-color pump-probe scheme to control the core polarization.

II. THEORETICAL MODEL

We consider a 1D atomic chain model based on TDDFT [47–51,53–55] in this work. This concise system can not only describe the interaction between lasers and solids at a level that encompasses multielectron effects but also allow for a clearer understanding of the underlying mechanisms. Specifically, we arrange N ions of charge Z in a linear fashion at positions

$$x_i = [i - (N+1)/2]a_0 \quad (i = 1, \ldots, N), \tag{1}$$

where a_0 is the lattice constant. The Kohn-Sham (KS) orbitals $\varphi_{i,\sigma}(x,t)$ satisfy the time-dependent KS equation

$$i\frac{\partial}{\partial t}\varphi_{i,\sigma}(x,t) = \left(-\frac{1}{2}\frac{\partial^2}{\partial x^2} + v_{\mathrm{KS}}[\{\rho_\sigma\}](x,t) - iA(t)\frac{\partial}{\partial x} + \frac{1}{2}A^2(t)\right)\varphi_{i,\sigma}(x,t), \tag{2}$$

where $v_{\mathrm{KS}}[\{\rho_\sigma\}](x,t)$ is the KS potential and $A(t)$ is the vector potential of the laser. The KS potential is composed of three components:

$$v_{\mathrm{KS}}[\{\rho_\sigma\}](x,t) = v_{\mathrm{ion}}(x) + u[\rho](x,t) + v_{\mathrm{xc}}[\{\rho_\sigma\}](x,t). \tag{3}$$

Here $v_{\mathrm{ion}}(x)$ is the ionic potential, $u[n](x,t)$ is the Hartree potential, and $v_{\mathrm{xc}}[\{\rho_\sigma\}](x,t)$ is the exchange-correlation potential in a local-spin-density approximation

$$v_{\mathrm{ion}}(x) = -\sum_{i=1}^{N}\frac{Z}{\sqrt{(x-x_i)^2+\epsilon}},$$
$$u[\rho](x,t) = \int\frac{\rho(x',t)dx'}{\sqrt{(x-x')^2+\epsilon}},$$
$$v_{\mathrm{xc}}[\{\rho_\sigma\}](x,t) \backsimeq -\left(\frac{6}{\pi}\rho_\sigma(x,t)\right)^{1/3}. \tag{4}$$

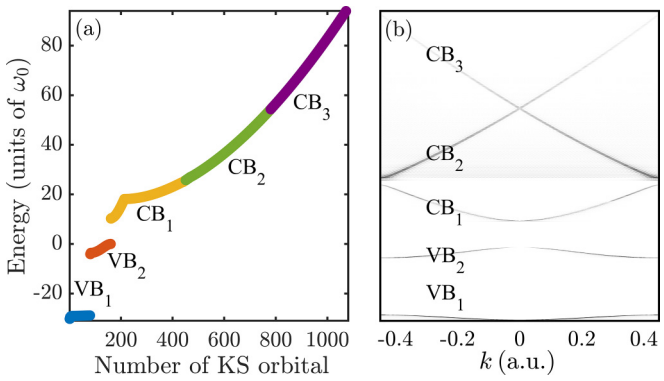

FIG. 1. Energy bands obtained from (a) the imaginary-time evolution in real space and (b) the Fourier transform of the ground-state KS orbitals in reciprocal space. The initially occupied bands are labeled VB$_i$ ($i = 1, 2$), while the initially unoccupied bands are labeled CB$_j$ ($j = 1, 2, 3$).

Here $\rho_\sigma(x,t)$ and $\rho(x,t)$ are the spin densities and the total density, respectively, written as

$$\rho_\sigma(x,t) = \sum_{i=1}^{N_\sigma}|\varphi_{\sigma,i}(x,t)|^2, \quad \rho(x,t) = \sum_{\sigma=\uparrow,\downarrow}\rho_\sigma(x,t), \tag{5}$$

where N_σ represents the number of electrons with spin $\sigma = \{\uparrow,\downarrow\}$ and $N_e = Z \times N = N_\uparrow + N_\downarrow$ is the total number of electrons. In the upcoming simulations, we consider a spin-neutral system ($N_\uparrow = N_\downarrow = N_e/2$) with the following parameters: the number of ions $N = 80$, the lattice constant $a_0 = 7$ a.u., the smoothing parameter $\epsilon = 2.25$, and the ion charge $Z = 4$. As discussed in Ref. [47], setting 40 ions in the laser polarization direction can already yield the converged bulk HHG spectrum. In addition, we also examine the results by increasing N to 220 and prove that the result of $N = 80$ converges. For brevity, we use the spin-restricted scheme and drop the spin index in the following formulation [53].

In order to obtain the ground-state KS orbitals of the system, we propagate the free-field KS equation in imaginary time. Based on the ground-state information, we analyze the band structures, as depicted in Fig. 1(a). By taking the Fourier transform of these eigenstates and combining the corresponding energy eigenvalues, we obtain the energy band structures in momentum space, as illustrated in Fig. 1(b). The five bands shown are labeled VB$_1$, VB$_2$, CB$_1$, CB$_2$, and CB$_3$. Orbitals 1–80 corresponding to VB$_1$ and orbitals 81–160 corresponding to VB$_2$ are the initially occupied KS orbitals within our system.

Then we employ the Crank-Nicolson method to numerically solve the time-dependent KS equations [56]. For the calculation, a grid spanning from -840 to 840 a.u. is employed, with the grid length being three times the chain length. The space step is set to $\Delta x = 0.1$ a.u. and the time step size is set to $\Delta t = 0.1$ a.u. After obtaining the time-dependent KS wave functions, we can obtain the total current generated by all the initially occupied orbitals

$$J(t) = \sum_i J_i(t), \tag{6}$$

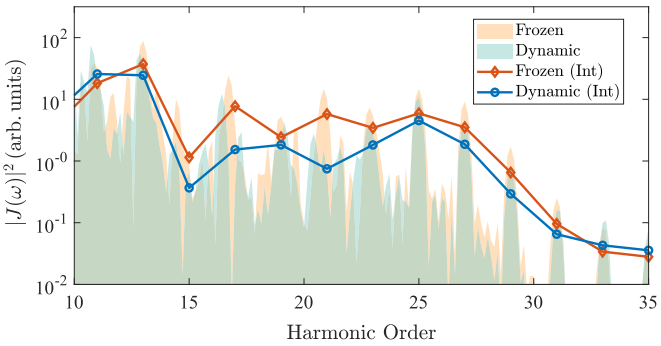

FIG. 2. Total HHG spectrum from all electrons. The area graphs represent the original data of the harmonic spectra, while the line plots illustrate the harmonic intensity after integrating the harmonics of each order.

where $J_i(t) = \langle \varphi_i(x,t)| - i\partial_x |\varphi_i(x,t)\rangle$ is the single-orbital current generated by an initially occupied KS orbital. The total HHG spectral intensity is then calculated as the modulus square of the Fourier-transformed total current

$$S(\omega) \propto |J(\omega)|^2 = \left| \int dt\, J(t) e^{-i\omega t} \right|^2. \tag{7}$$

The laser field used in all ensuing calculations is described by the vector potential unless otherwise stated,

$$A(t) = A_0 f(t) \sin(\omega_0 t), \tag{8}$$

where $A_0 = 0.26$ a.u. is the amplitude and $\omega_0 = 0.023$ a.u. is the frequency, approximately one-tenth of the band-gap energy of our studied system. The optical field has a duration of $\tau = 7T_0$ (T_0 is the optical cycle of the driving laser) and is enveloped by a trapezoidal shape $f(t)$, with both the rising and falling edges each lasting $2T_0$.

During dynamic time-dependent evolution, the KS potential $v_{\mathrm{KS}}[\{\rho\}](x,t)$ is dynamically updated based on the redistributed dynamics of the electron density $\rho(t)$ at each step. We simulate the polarization of the core in the laser field using this approach, which we refer to as "Dynamic" in the subsequent discussion. As a comparative benchmark to the dynamic core model, the KS potential is held fixed in the simulation, constraining electrons to evolve independently within the static potential of the ground state

$$v_{\mathrm{KS}}[\{\rho\}](x,t) \backsimeq v_{\mathrm{KS}}[\{\rho\}](x,0) = v_{\mathrm{KS}}^{\mathrm{GS}}. \tag{9}$$

This modeling strategy effectively simulates a frozen core scenario, referred to as the "Frozen" simulation. The disparity in the level of describing the electron dynamics encompassed by these two calculation methods allows us to get insight into the impact of core-polarization effects.

III. RESULTS AND DISCUSSION

During our investigation, we focus on examining the impact of core polarization on the total HHG. In Fig. 2 we present the total harmonic spectrum generated by all electrons, revealing notable differences between "Dynamic" and "Frozen" scenarios. The area graphs represent the raw data of the harmonic spectra, while the line plots depict the harmonic intensity within each odd-order harmonic. Each point on the dotted line is calculated by integrating the intensity of all harmonics within half an order before and after that order. This representation more accurately captures the trends in harmonic intensity between adjacent orders and provides a clearer comparison of the same-order harmonics between "Frozen" and "Dynamic" simulations. Comparing the results between the "Dynamic" and "Frozen" simulations, the harmonic intensity in the first plateau region is several times higher in the "Frozen" simulation. The result is the same in the simulation of $N = 220$.

A. Subshell polarization approach: Distinguishing the effects of polarization from different shells

In the calculations of Fig. 2, the description of the core polarization encompasses the whole core, as has been the case in previous work. However, as mentioned in Sec. II, our model encompasses 160 orbitals, with orbitals 1–80 corresponding to VB_1 and orbitals 81–160 corresponding to VB_2. Thus, we can consider the density of the core as consisting of two distinct parts: $\rho_1(x,t)$ for electrons in VB_1 (inner-shell electrons) and $\rho_2(x,t)$ for electrons in VB_2 (outer-shell electrons). These can be mathematically represented as

$$\rho_1(x,t) = 2\sum_{i=1}^{i=80} |\varphi_i(x,t)|^2, \quad \rho_2(x,t) = 2\sum_{i=81}^{i=160} |\varphi_i(x,t)|^2, \tag{10}$$

where the factor 2 accounts for the spin degeneracy. The total density can be expressed as the sum of the two, i.e., $\rho(x,t) = \rho_1(x,t) + \rho_2(x,t)$. For convenience, we omit the spatial variable x in the subsequent discussion involving the density, denoting the densities by $\rho(t)$, $\rho_1(t)$, and $\rho_2(t)$, respectively.

Therefore, it is necessary to study the polarization effects of different shells on the results and the mechanism of their influence, respectively. To distinguish the effects of polarization from different shells, we propose a subshell polarization approach. First, we perform a complete TDDFT calculation to obtain the time evolution of the total electronic density $\rho(t)$, which is then partitioned into $\rho_1(t)$ and $\rho_2(t)$ according to Eq. (10). Here $\rho_1(t)$ and $\rho_2(t)$ contain the dynamic information of electrons in the two valence bands under the applied laser field. Consequently, we can construct two types of total density: One is $\rho_1(t) + \rho_2(0)$, which combines the time-dependent density of inner-shell electrons evolving during the TDDFT simulation and the static density of outer-shell electrons in the ground states; the other is $\rho_1(0) + \rho_2(t)$, combining the time-dependent density of outer-shell electrons evolving during the TDDFT simulation and the static density of inner-shell electrons in the ground states. Based on Eqs. (3) and (4), we encapsulate the core-polarization effects involving contributions from different valence shells into time-dependent effective KS potentials, denoted by $v_{\mathrm{KS}}[\rho_1(t) + \rho_2(0)]$ and $v_{\mathrm{KS}}[\rho_1(0) + \rho_2(t)]$. Subsequently, we recalculate the wave functions $\varphi_i(t)$ under the

above two potentials, respectively, by solving the TDSE as

$$i\partial_t\varphi_i(t) = \left(-\frac{1}{2}\frac{\partial^2}{\partial x^2} + v_{\mathrm{KS}}[\rho_1(t)+\rho_2(0)] + H_I(t)\right)\varphi_i(t),$$
$$i\partial_t\varphi_i(t) = \left(-\frac{1}{2}\frac{\partial^2}{\partial x^2} + v_{\mathrm{KS}}[\rho_1(0)+\rho_2(t)] + H_I(t)\right)\varphi_i(t), \tag{11}$$

where the time-dependent $H_I(t) = -iA(t)\frac{\partial}{\partial x} + \frac{1}{2}A^2(t)$ describes the effect of the external laser field. Finally, by including Eq. (6), we can obtain the total current.

It is worth noting that, by using the subshell polarization approach above, we can selectively exclude the direct core-polarization effects of one specific shell on HHG. In this scenario, the electron dynamics in one shell still has an effect on the electrons in the other shell during the evolution, because of the time-dependent potential $v_{\mathrm{KS}}(t)$. For instance, in the case of $v_{\mathrm{KS}}[\rho_1(0)+\rho_2(t)]$, although the influence of the inner-shell core polarization is eliminated by replacing $\rho_1(t)$ with $\rho_1(0)$, the dynamics of these electrons might be widely different because of the dynamic interaction from the outer electrons. As this work concerns direct core-polarization effects on HHG rather than the multielectron interaction effects, the subshell polarization approach offers a precisely suited method for the current discussion.

Similarly, when both the inner- and outer-shell electrons are eliminated, we have $\rho_1(0)+\rho_2(0) = \rho(0)$, and when both are taken into account, we have $\rho_1(t)+\rho_2(t) = \rho(t)$. The corresponding potentials are $v_{\mathrm{KS}}[\rho(0)]$ and $v_{\mathrm{KS}}[\rho(t)]$, respectively. It has been verified that the results from the "Dynamic" and "Frozen" simulations based on TDDFT are identical to those obtained using the TDSE with the effective potentials $v_{\mathrm{KS}}[\rho(t)]$ and $v_{\mathrm{KS}}[\rho(0)]$, respectively. This consistency serves as a crucial justification for the validity of this separation approach. In Secs. III B and III C we apply this method for deeper analysis.

B. Characterization of harmonic suppression induced by core polarization

The harmonic suppression of the "Dynamic" scenario compared to the "Frozen" corroborates previous findings indicating that the SAE approximation tends to overestimate the electric field acting on electrons, thereby leading to less precise predictions of harmonic spectra. This observation is generally elucidated through the lens of local-field effects in solid-state physics. When subjected to an external electric field, electrons undergo core polarization, resulting in localized fluctuations in electron density. These fluctuations induce an electric field that partially counteracts the applied laser field, effectively reducing the total electric field experienced by the electrons responsible for harmonic generation.

Previous works have often overlooked a detailed analysis of the suppression characteristics. In this section we investigate the impact of polarization of different shells on this phenomenon with the subshell polarization approach.

First, we present in Fig. 3 the harmonic spectra from four simulations. From Fig. 3(a) it is evident that the result from $J[\rho_1(0)+\rho_2(t)]$ is more similar to the "Dynamic"

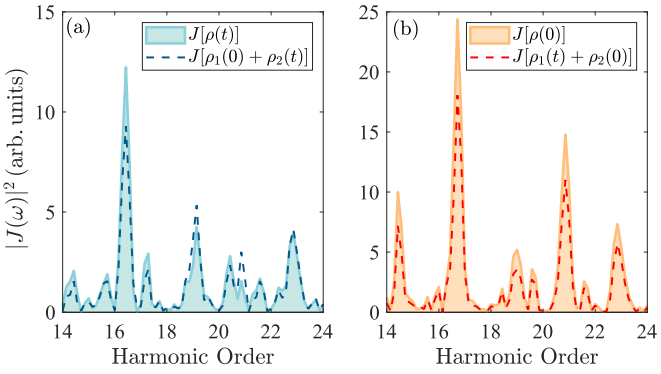

FIG. 3. Harmonics generated from all electrons in the first plateau region. Results are compared from (a) $J[\rho(t)]$ and $J[\rho_1(0)+\rho_2(t)]$ and (b) $J[\rho(0)]$ and $J[\rho_1(t)+\rho_2(0)]$.

simulation result $J[\rho(t)]$. From Fig. 3(b) we see that the harmonic spectrum from $J[\rho_1(t)+\rho_2(0)]$ matches better with the "Frozen" result $J[\rho(0)]$. This suggests that the dynamic evolution of $\rho_2(t)$ plays an important role in the screening, while $\rho_1(t)$ also contributes but to a lesser extent.

To shed light on the results above, we present the polarization of the two shells in Fig. 4. In Fig. 4(a) we illustrate the difference between the electron density at a certain moment [denoted by the purple dashed lines in Figs. 4(b) and 4(c)] and the ground-state electron density. Specifically, $\Delta\rho_1(t) = \rho_1(t) - \rho_1(0)$, $\Delta\rho_2(t) = \rho_2(t) - \rho_2(0)$, and $\Delta\rho(t) = \rho(t) - \rho(0)$. Notably, $\Delta\rho_2(t)$ exhibits an order of magnitude larger variation than $\Delta\rho_1(t)$, thereby exerting a dominant influence on the variations of $\Delta\rho(t)$. Figures 4(b) and 4(c) display the electron density fluctuations of ρ_1 and ρ_2, respectively, within one unit cell over the third to the fourth optical cycles. It is noticeable that $\Delta\rho_1$ exhibits clear high-frequency components, which can also be seen in $\Delta\rho_2$. This is due to the nonadiabatic laser-induced electron dynamics. It is also shown that the fluctuation of ρ_2 is larger than ρ_1. This can be understood by the fact that $\rho_2(t)$, corresponding to the more active outer valence electrons, is more sensitive to external fields.

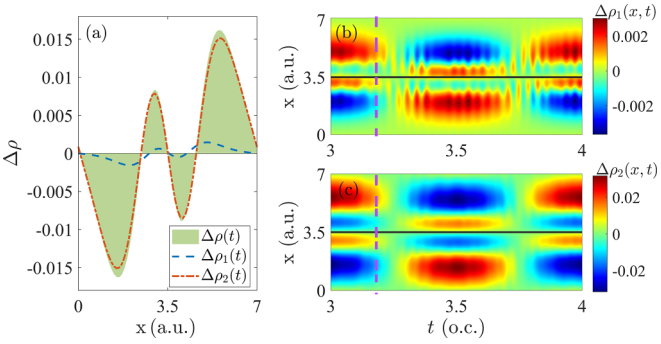

FIG. 4. (a) Difference between the electron density at a certain moment [denoted by the purple dashed lines in (b) and (c)] and the ground-state electron density in a cell. (b) Density fluctuations of the inner-shell electrons $\Delta\rho_1(t)$ in the dynamic simulation as a function of time and space. (c) Density fluctuations of the outer-shell electrons $\Delta\rho_2(t)$ in the dynamic simulation. The black solid line indicates the position of the nucleus.

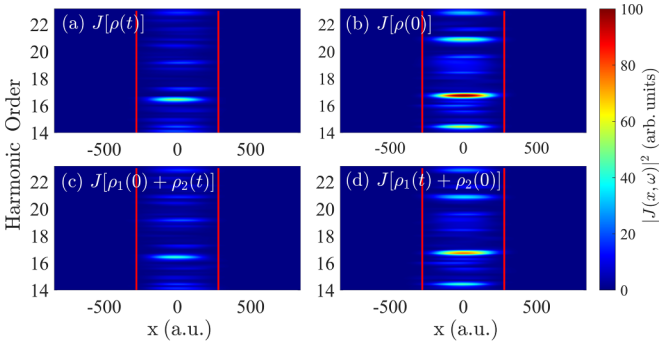

FIG. 5. Spatial-frequency spectrogram of harmonics generated from all electrons, with results calculated from (a) $J[\rho(t)]$, (b) $J[\rho(0)]$, (c) $J[\rho_1(0)+\rho_2(t)]$, and (d) $J[\rho_1(t)+\rho_2(0)]$. The red lines indicate the boundaries of the linear chain of atoms.

Meanwhile, $\rho_1(t)$, corresponding to electrons in the inner valence band, experiences tighter confinement and undergoes lesser excitation under the laser field. Thus, the polarization of ρ_2 has a more significant impact on the harmonics, as shown in Fig. 3(a).

Next we aim to examine the spatial distribution of harmonics from the 14th to the 24th order from different shell polarization. Specifically, we employ

$$J(x_i,\omega)=\mathcal{F}\left(\int_x\sum_j[-i\varphi_j^*(x,t)\partial_x\varphi_j(x,t)]W(x,x_i,\sigma^2)dx\right), \tag{12}$$

where $\mathcal{F}$ denotes the Fourier transform and $W(x,x_i,\sigma^2)$ is a normalized Gaussian function with expected value x_i and variance $\sigma^2=(\frac{40}{3}a_0)^2$. By applying Eq. (12), we can obtain a 2D spectrogram of the harmonic intensity $S(x_i,\omega)=|J(x_i,\omega)|^2$ as a function of the radiation position and harmonic order and then achieve the purpose of analyzing the spatial distribution of harmonics. The results are shown in Fig. 5. It can be seen that the primary contributions of harmonics are concentrated in the central region of the model chain. From Figs. 5(a) and 5(b) we see that the peak intensity of the spatial distribution of $J[\rho(0)]$ is approximately twice as high as that of $J[\rho(t)]$, consistent with the results in the total harmonic spectra. Meanwhile, the suppression in the "Dynamic" simulation is uniform across the spatial distribution. From Figs. 5(c) and 5(d) we see that the effects of $\rho_1(t)$ and $\rho_2(t)$ on the harmonic radiation in the first plateau region are also spatially homogeneous, suggesting that the two have a mechanistically consistent but magnitudinally different influence on the suppression phenomenon.

Previous studies have suggested that significant local-field effects occur when the defected solids are driven by lasers [32]. This phenomenon also arises when the materials' surfaces are driven by out-of-plane external fields [30,57]. However, strong local-field effects are not observed in crystals like Si, MgO, and h-BN [29,32,58]. While our study aims to simulate electrons driven in the polarization direction of a linearly polarized laser in bulk crystals, the model is still a finite-length chain rather than a strictly periodic system.

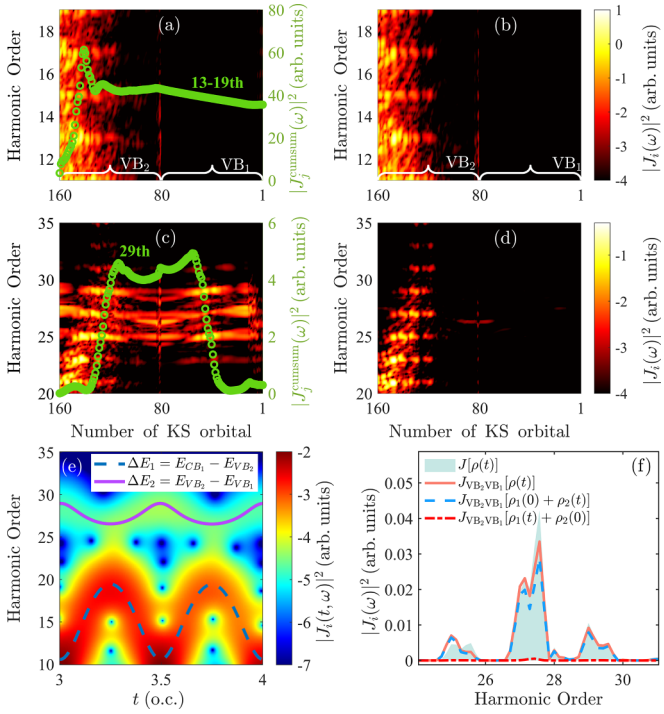

FIG. 6. The harmonic yield of different occupied KS orbitals for different regions is plotted with a logarithmic color scale: (a) and (b) the first plateau outside the peak region and (c) and (d) the peak region. The open circles indicate the harmonic intensity $|J_j^{\rm cumsum}(\omega)|^2$ from the coherent superposition of contributions by orbitals with higher orbital index, namely, higher energies, than the corresponding horizontal value. (e) Time-frequency spectrogram for the contribution of orbital 160 with a logarithmic color scale calculated by dynamic simulation. The purple solid curve and the blue dashed curve correspond to the energy differences $\Delta E_1(t)$ and $\Delta E_2(t)$, respectively. (f) Harmonics generated from orbital 160.

C. Analysis of the harmonic peak in dynamic simulations

In addition to the harmonic suppression, examining the result from the "Dynamic" simulation, we can notice a peak around the 25th order, which corresponds to the energy gap between VB_1 and VB_2. In contrast, the result from the "Frozen" simulation shows a flat first plateau with no peaks in this region at all. To understand this phenomenon, we plot the harmonic yield contributed by different KS orbitals (orbitals 1–80 correspond to VB_1, while orbitals 81–160 correspond to VB_2) to the harmonic yield $|J_i(\omega)|^2$ for different regions in Figs. 6(a)–6(d). Figures 6(a) and 6(b) and Figs. 6(c) and 6(d) correspond to spectral ranges in the first plateau outside and in the peak region, respectively, and Figs. 6(a) and 6(c) and Figs. 6(b) and 6(d) correspond to the "Dynamic" and "Frozen" results, respectively. We acknowledge that splitting the physical observable total spectrum into contributions from each single orbital falls beyond the assurance of DFT, and the single-electron results are not observable quantities. However, the remarkable distinct feature shown in Fig. 6(c) suggests that this analysis method may serve as a tool to inspire a possible intuitive physical picture behind the phenomenon.

Specifically, Figs. 6(a) and 6(b) show that the dominant contribution to the first plateau of the harmonic spectrum orig-

inates from electrons initially located in the highest valence band VB_2, which is consistent with previous studies. The electrons in the inner valence band VB_1 have lower energies and therefore make less significant contributions to the first plateau. On the other hand, within the peak region shown in Figs. 6(c) and 6(d), three distinct horizontal lines are evident in Fig. 6(c), signifying that in "Dynamic" calculations, the harmonics generated by each initially occupied KS orbital are enhanced around the corresponding 25th to 30th orders. However, the "Frozen" results in Fig. 6(d) are mainly contributed by VB_2. To examine in more detail the unique results shown in Fig. 6(c), we take one specific slice (orbital index $i = 160$) for further discussion.

Figure 6(e) displays the time-frequency spectrogram for the contribution of orbital 160 calculated by the "Dynamic" simulation using the Gabor transform of $J_i(t)$ [59]. The spectrogram includes a channel corresponding to the instantaneous energy differences of VB_2 and CB_1, according to the acceleration theorem $\Delta E_1(t) = E_{CB_1}[A(t)] - E_{VB_2}[A(t)]$, where the initial KS orbital 160 is located around $k_0 = 0$ in momentum space. This HHG channel results from the interband transition between CB_1 and VB_2 [47]. More importantly, the "Dynamic" simulation exhibits an additional channel, which is almost completely disallowed in the "Frozen" simulations. The additional channel corresponds to the instantaneous energy differences of two valence bands $\Delta E_2(t) = E_{VB_2}[A(t)] - E_{VB_1}[A(t)]$. This implies that the peak in the harmonic spectrum, present in the "Dynamic" simulation, is associated with the coupling between valence bands, and core polarization may profoundly alter the electron dynamics within these bands.

By inserting the complete orthogonal set consisting of static KS orbitals into the calculation for J_i, we have $J_i(t) = \sum_{m,n} \langle\varphi_i(t)\rangle \varphi_m^{GS} \langle\varphi_m^{GS}| - i\partial_x |\varphi_n^{GS}\rangle \langle\varphi_n^{GS}\rangle \varphi_i(t) = \sum_{m,n} c_m^*(t)c_n(t)T_{mn}$, where m (n) represents the mth (nth) ground-state KS orbital, $c_m(t) = \langle\varphi_m^{GS}\rangle \varphi_i(t)$ are the time-dependent projections of $|\varphi_i(t)\rangle$ on $|\varphi_m^{GS}\rangle$, and $T_{mn} = \langle\varphi_m^{GS}| - i\partial_x |\varphi_n^{GS}\rangle$ are the transition matrix elements. Based on the result of time-frequency analysis, we consider the current contribution from the coupling of VB_1 and VB_2,

$$J_{VB_1VB_2}(t) = \sum_{m,n\in VB_1,VB_2} c_m^*(t)c_n(t)T_{mn} = J_{VB_1VB_2} + J_{VB_2VB_1} + J_{VB_1VB_1} + J_{VB_2VB_2}, \quad (13)$$

where $J_{VB_aVB_b} = \sum_{m\in VB_a, n\in VB_b} c_m^*(t)c_n(t)T_{mn}$.

Combined with the subshell polarization approach in Sec. III A, we calculate the corresponding HHG in "Dynamic" simulations, as shown in Fig. 6(f). Comparing the single-electron HHG (area plot) with the harmonic calculated from the separated $J_{VB_2VB_1}$ channel (pink solid line), we can see that the interband current $J_{VB_2VB_1}$ primarily accounts for the peak. Meanwhile, in Fig. 6(f) the three line plots demonstrate the effect of different degrees of core polarization to this channel. It is evident that the results of $J_{VB_2VB_1}[\rho_1(0) + \rho_2(t)]$ and $J_{VB_2VB_1}[\rho(t)]$ exhibit remarkable consistency. However, the harmonic yield of $J_{VB_2VB_1}[\rho_1(t) + \rho_2(0)]$ is relatively weak compared to $J_{VB_2VB_1}[\rho_1(0) + \rho_2(t)]$, and the additional peak in the harmonic spectrum disappears. It is more similar to the "Frozen" simulation result. This suggests that the polarization of electrons from the outer shell mainly contributes to the peak, consistent with the discussion in Fig. 4.

However, what is actually observable is the total harmonic spectrum, the accumulation of individual orbital contributions. Therefore, we go further to use Fig. 6(c) as a backdrop, overlaid with the harmonic intensity (represented by the circles) $|J_j^{cumsum}(\omega)|^2 = |\int dt \sum_{i=j}^{160} J_i(t)e^{-i\omega t}|^2$, which is the coherent sum of contributions from different orbitals from the number of KS orbitals j (corresponding to the horizontal axis) to 160. Here we consider the result of the 29th harmonic as representative of the harmonics in the peak region. As a comparison, we also display the results for the 13th to 19th orders in Fig. 6(a). From the green open circles in Fig. 6(a), it is evident that the total harmonic yield in the first plateau region increases significantly when the contributions from orbitals 81–160 are cumulated. Naturally, it remains relatively constant when cumulating the contribution from orbitals 1–80. This contrasts significantly with the interference phenomenon observed at the 29th harmonic, as depicted in Fig. 6(c). Despite the considerable contribution from electrons in VB_1 to the 29th harmonic, the contributions from VB_1 and VB_2 symmetrically cancel during the interference process.

This result is due to the inherent feature of the 1D model we use. In the completely filled valence bands, roughly one-half of the KS electrons with positive band curvature move oppositely to the other half with negative band curvature. The contributions of KS orbitals undergo destructive interference and cancellation due to the opposite curvature [47,48]. Meanwhile, it is worth noting that the signal of VB_2-CB_1 coupling [still present in Fig. 6(d)] also contributes to the peak region in the spectrum. Therefore, the total harmonic spectrum is also influenced by the interference between VB_2-CB_1 and VB_1-VB_2 channels, which cannot be simply understood based on the coupling of valence bands. These interference effects between many orbitals ultimately diminish the peaks of harmonics in the "Dynamic" simulation, making the peaks in the observable total HHG less prominent. Nevertheless, the above analysis suggests a possible physical picture that the peak is related to the additional contributing VB_1-VB_2 channel in the present of core polarization. However, this analysis is not rigorous enough to draw a definitive conclusion, and further research is required.

D. Controlling core-polarization effects through the two-color pump-probe scheme

As discussed in the preceding section, the local-field effect is an effect accompanying core polarization, primarily contributed by the outer-shell electrons. However, this does not imply that considering only the dynamics of outer valence electrons applies universally. It was mentioned in Ref. [49] that neglecting electrons in the inner valence may affect the results. Given that the polarization of the inner electrons is relatively weak, one effective way to enhance core polarization is to promote the polarization of inner-shell electrons. Consequently, we employ a two-color pump-probe scheme [49,60,61], where a UV preexcitation pumps electrons from VB_1 to CB_1 followed by a midinfrared (MIR) pulse to drive the core polarization. It has been shown that this method can trigger significant laser-induced correlations. As a

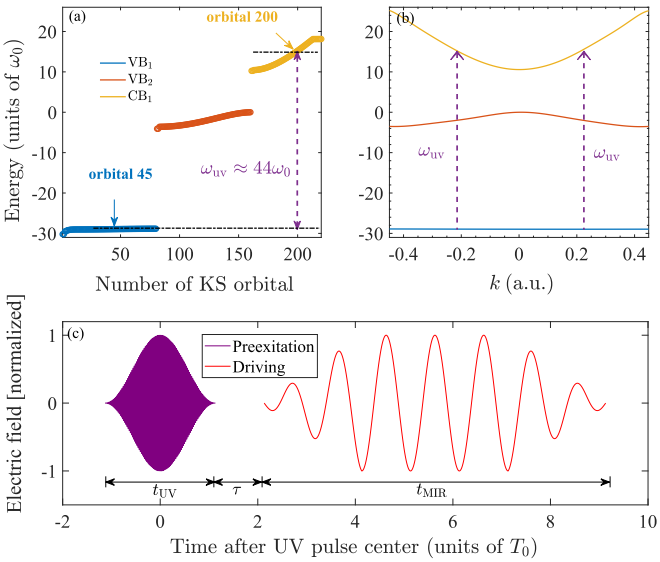

FIG. 7. Schematic of the UV excitation in the (a) real-space and (b) momentum-space band structure, with the purple arrows indicating the excitation of electrons from VB_1 to CB_1 by the UV pulse. (c) Electric field of the two-color pump-probe scheme in units of the period T_0 of the MIR field, with each pulse individually normalized.

demonstration, we consider a UV laser pulse with the frequency corresponding to the energy difference between VB_1 and CB_1, as shown in Fig. 7(a). Correspondingly, we also depict the schematic of the UV preexcitation in the k space in Fig. 7(b), with the purple arrows indicating the UV pulse exciting electrons from VB_1 to CB_1 at $k \approx 0.22$. Specifically, the combined vector potential field is

$$A(t) = A_{UV}(t) + A_{MIR}(t), \tag{14}$$

with the explicit forms

$$A_{UV}(t) = A_{UV}\sin^2\left(\frac{\pi t}{t_{UV}}\right)\sin(\omega_{UV}t), \quad 0 < t < t_{UV}$$
$$A_{MIR}(t) = A_{MIR}f(t-\tau-t_{UV})\sin[\omega_{UV}(t-\tau-t_{UV})],$$
$$t_{UV}+\tau < t < t_{UV}+\tau+t_{MIR}. \tag{15}$$

Here $\omega_{UV} = 1.0164$ a.u. is the frequency of the UV pulse, $A_{UV} = 0.026$ a.u. is the UV pulse amplitude, and the duration time of the UV pulse is set as $t_{UV} = 14.8$ fs. For the MIR driving pulse, the frequency $\omega_{MIR} = \omega_0$, the amplitude $A_{MIR} = 0.26$ a.u., and the duration time is set as $t_{MIR} = 45.9$ fs. Furthermore, τ is the time delay between the two pulses. The corresponding two-color pump-probe pulse sequence is illustrated in Fig. 7(c).

Based on the aforementioned two-color pump-probe scheme, we calculate the corresponding total harmonic spectra combined with the subshell polarization approach, as shown in Fig. 8. It is evident from the results that both $J[\rho_1(t)+\rho_2(0)]$ and $J[\rho_1(0)+\rho_2(t)]$ exhibit significant deviations from the dynamic result $J[\rho(t)]$. This discrepancy is clearer in the integrated point-line plots. With the excitation of inner-shell electrons by the UV pulse, the dynamic evolution of $\rho_1(t)$ becomes notably enhanced and cannot be neglected. Laser-induced polarization manifests prominently in both

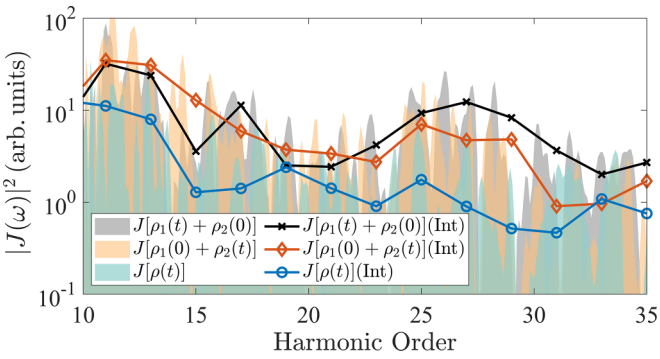

FIG. 8. Total HHG spectrum from all electrons with the two-color pump-probe scheme. The area graphs represent the original data of the harmonic spectra, while the line plots illustrate the harmonic intensity after integrating the harmonics of each order.

electron shells, indicating that considering solely the dynamics of outer-shell electrons is insufficient to fully describe the system's dynamics under the laser field. By employing this approach, we successfully manipulate and modulate the core-polarization effects.

IV. CONCLUSION

Our study has systematically investigated the core-polarization effects in HHG. Through TDDFT simulations, we found that core polarization induces a suppression of HHG in the first plateau region. To delve into the roles of different shells, we proposed a subshell polarization approach to distinguish the effects of core polarization from a specific shell. Using this approach, we provided detailed analysis of the suppression characteristics, confirming that the core polarization of the outer shell has a dominant contribution. Meanwhile, we analyzed the harmonic peaks around the 25th order in the "Dynamic" simulation and proposed a possible physical explanation that core polarization alters electron dynamics and facilitates the coupling between the valence bands. Moreover, based on the aforementioned study, we proposed to control core polarization through a two-color pump-probe scheme by facilitating the core polarization of the inner shell.

Overall, our study provides comprehensive insights into the mechanisms underlying core-polarization effects in HHG and enhances our understanding of the intricate electron dynamics in solids. The core-polarization effect occurs within the timescale of the external driving field. This implies a new freedom of manipulating the optical response of materials using strong laser fields.

ACKNOWLEDGMENTS

This work was supported by National Key Research and Development Program (Grants No. 2023YFA1406800 and No. 2022YFA1604403) and the National Natural Science Foundation of China (Grants No. 12174134, No. 12104172, No. 12021004, and No. 12374317). The computation was completed on the HPC Platform of Huazhong University of Science and Technology.

[1] P. B. Corkum, Phys. Rev. Lett. **71**, 1994 (1993).
[2] T. Brabec and F. Krausz, Rev. Mod. Phys. **72**, 545 (2000).
[3] P. B. Corkum and F. Krausz, Nat. Phys. **3**, 381 (2007).
[4] F. Krausz and M. Ivanov, Rev. Mod. Phys. **81**, 163 (2009).
[5] S. Ghimire, A. D. DiChiara, E. Sistrunk, P. Agostini, L. F. DiMauro, and D. A. Reis, Nat. Phys. **7**, 138 (2011).
[6] A. Schiffrin, T. Paasch-Colberg, N. Karpowicz, V. Apalkov, D. Gerster, S. Mühlbrandt, M. Korbman, J. Reichert, M. Schultze, S. Holzner, J. V. Barth, R. Kienberger, R. Ernstorfer, V. S. Yakovlev, M. I. Stockman, and F. Krausz, Nature (London) **493**, 70 (2013).
[7] O. Schubert, M. Hohenleutner, F. Langer, B. Urbanek, C. Lange, U. Huttner, D. Golde, T. Meier, M. Kira, S. W. Koch, and R. Huber, Nat. Photonics **8**, 119 (2014).
[8] C. R. McDonald, G. Vampa, P. B. Corkum, and T. Brabec, Phys. Rev. Lett. **118**, 173601 (2017).
[9] R. R. Alfano and S. F. B. Mazhar, Sci. Rep. **13**, 15467 (2023).
[10] T. J. Hammond, S. Monchocé, C. Zhang, G. Vampa, D. Klug, A. Y. Naumov, D. M. Villeneuve, and P. B. Corkum, Nat. Photonics **11**, 594 (2017).
[11] T. T. Luu, M. Garg, S. Y. Kruchinin, A. Moulet, M. T. Hassan, and E. Goulielmakis, Nature (London) **521**, 498 (2015).
[12] H. Kim, S. Han, Y. W. Kim, S. Kim, and S.-W. Kim, ACS Photonics **4**, 1627 (2017).
[13] M. Garg, H. Y. Kim, and E. Goulielmakis, Nat. Photonics **12**, 291 (2018).
[14] G. Vampa, T. J. Hammond, N. Thiré, B. E. Schmidt, F. Légaré, C. R. McDonald, T. Brabec, D. D. Klug, and P. B. Corkum, Phys. Rev. Lett. **115**, 193603 (2015).
[15] A. A. Lanin, E. A. Stepanov, A. B. Fedotov, and A. M. Zheltikov, Optica **4**, 516 (2017).
[16] C. Yu, S. Jiang, T. Wu, G. Yuan, Z. Wang, C. Jin, and R. Lu, Phys. Rev. B **98**, 085439 (2018).
[17] L. Li, P. Lan, L. He, W. Cao, Q. Zhang, and P. Lu, Phys. Rev. Lett. **124**, 157403 (2020).
[18] M. Hohenleutner, F. Langer, O. Schubert, M. Knorr, U. Huttner, S. W. Koch, M. Kira, and R. Huber, Nature (London) **523**, 572 (2015).
[19] N. Rana, M. S. Mrudul, D. Kartashov, M. Ivanov, and G. Dixit, Phys. Rev. B **106**, 064303 (2022).
[20] X. Song, S. Yang, G. Wang, J. Lin, L. Wang, T. Meier, and W. Yang, Opt. Express **31**, 18862 (2023).
[21] J. Liang, Y. Zhou, Y. Liao, W.-C. Jiang, M. Li, and P. Lu, Ultrafast Sci. **2022**, 9842716 (2022).
[22] T. T. Luu and H. J. Wörner, Phys. Rev. B **94**, 115164 (2016).
[23] J. Li, X. Zhang, S. Fu, Y. Feng, B. Hu, and H. Du, Phys. Rev. A **100**, 043404 (2019).
[24] B.-H. Lei, S. Pan, Z. Yang, C. Cao, and D. J. Singh, Phys. Rev. Lett. **125**, 187402 (2020).
[25] Y. Lang, Z. Peng, J. Liu, Z. Zhao, and S. Ghimire, Phys. Rev. Lett. **129**, 167402 (2022).
[26] M. Wu, D. A. Browne, K. J. Schafer, and M. B. Gaarde, Phys. Rev. A **94**, 063403 (2016).
[27] J.-Q. Liu and X.-B. Bian, Phys. Rev. Lett. **127**, 213901 (2021).
[28] T.-J. Shao, Q.-L. Zhang, Y.-D. Song, and H.-Q. Zou, J. Phys. B **56**, 165401 (2023).
[29] N. Tancogne-Dejean, O. D. Mücke, F. X. Kärtner, and A. Rubio, Phys. Rev. Lett. **118**, 087403 (2017).
[30] N. Tancogne-Dejean and A. Rubio, Sci. Adv. **4**, eaao5207 (2018).
[31] N. Tancogne-Dejean, M. A. Sentef, and A. Rubio, Phys. Rev. Lett. **121**, 097402 (2018).
[32] M. S. Mrudul, N. Tancogne-Dejean, A. Rubio, and G. Dixit, NPJ Comput. Mater. **6**, 10 (2020).
[33] O. Neufeld, N. Tancogne-Dejean, H. Hübener, U. De Giovannini, and A. Rubio, Phys. Rev. X **13**, 031011 (2023).
[34] T. Ikemachi, Y. Shinohara, T. Sato, J. Yumoto, M. Kuwata-Gonokami, and K. L. Ishikawa, Phys. Rev. A **98**, 023415 (2018).
[35] A. Trautmann, R. Zuo, G. Wang, W.-R. Hannes, S. Yang, L. H. Thong, C. Ngo, J. T. Steiner, M. Ciappina, M. Reichelt, H. T. Duc, X. Song, W. Yang, and T. Meier, in *Proceedings of the Conference on Ultrafast Phenomena and Nanophotonics XXVI, San Francisco, 2022*, edited by M. Betz and A. Y. Elezzabi (SPIE, Bellingham, 2022).
[36] B. Zhang, J. Yuan, and Z. Zhao, Phys. Rev. Lett. **111**, 163001 (2013).
[37] J. Rapp and D. Bauer, Phys. Rev. A **89**, 033401 (2014).
[38] S. G. Walt, N. Bhargava Ram, M. Atala, N. I. Shvetsov-Shilovski, A. von Conta, D. Baykusheva, M. Lein, and H. J. Worner, Nat. Commun. **8**, 15651 (2017).
[39] N. I. Shvetsov-Shilovski, M. Lein, and L. B. Madsen, Phys. Rev. A **98**, 023406 (2018).
[40] M. Abu-samha and L. B. Madsen, Phys. Rev. A **101**, 013433 (2020).
[41] S. Hu, Z. Shu, L. Guo, and J. Chen, Phys. Rev. A **104**, 043110 (2021).
[42] M. Abu-samha and L. B. Madsen, Phys. Rev. A **106**, 013117 (2022).
[43] H. T. Nguyen, K.-N. H. Nguyen, N.-L. Phan, C.-T. Le, D. Vu, L.-P. Tran, and V.-H. Le, Phys. Rev. A **105**, 023106 (2022).
[44] C.-T. Le, C. Ngo, N.-L. Phan, D. Vu, and V.-H. Le, Phys. Rev. A **107**, 043103 (2023).
[45] K. Chordiya, V. Despré, B. Nagyillés, F. Zeller, Z. Diveki, A. I. Kuleff, and M. U. Kahaly, Phys. Chem. Chem. Phys. **25**, 4472 (2023).
[46] L. He, Y. He, S. Sun, E. Goetz, A.-T. Le, X. Zhu, P. Lan, P. Lu, and C.-D. Lin, Adv. Photonics **5**, 056001 (2023).
[47] K. K. Hansen, T. Deffge, and D. Bauer, Phys. Rev. A **96**, 053418 (2017).
[48] D. Bauer and K. K. Hansen, Phys. Rev. Lett. **120**, 177401 (2018).
[49] S. V. B. Jensen and L. B. Madsen, Phys. Rev. B **104**, 054309 (2021).
[50] C. Yu, K. K. Hansen, and L. B. Madsen, Phys. Rev. A **99**, 063408 (2019).
[51] C. Yu, K. K. Hansen, and L. B. Madsen, Phys. Rev. A **99**, 013435 (2019).
[52] L. Li, Y. Zhang, P. Lan, T. Huang, X. Zhu, C. Zhai, K. Yang, L. He, Q. Zhang, W. Cao, and P. Lu, Phys. Rev. Lett. **126**, 187401 (2021).
[53] C. Yu, H. Iravani, and L. B. Madsen, Phys. Rev. A **102**, 033105 (2020).
[54] J.-Q. Liu and X.-B. Bian, Phys. Rev. B **102**, 174302 (2020).
[55] C. Yu, U. Saalmann, and J. M. Rost, Phys. Rev. A **106**, 013105 (2022).

[56] *Computational Strong-Field Quantum Dynamics*, edited by D. Bauer (de Gruyter, Berlin, 2017).

[57] G. Le Breton, A. Rubio, and N. Tancogne-Dejean, Phys. Rev. B **98**, 165308 (2018).

[58] N. Tancogne-Dejean, O. D. Mücke, F. X. Kärtner, and A. Rubio, Nat. Commun. **8**, 745 (2017).

[59] C. C. Chirilă, I. Dreissigacker, E. V. van der Zwan, and M. Lein, Phys. Rev. A **81**, 033412 (2010).

[60] S. V. B. Jensen, H. Iravani, and L. B. Madsen, Phys. Rev. A **103**, 053121 (2021).

[61] N. Sun, X. Zhu, L. Li, P. Lan, and P. Lu, Phys. Rev. A **103**, 053111 (2021).